

The Hurst Exponent of Fermi GRBs

G. A. MacLachlan^{1*}, A. Shenoy¹, E. Sonbas^{2,3}, R. Coyne¹, K. S. Dhuga¹,
A. Eskandarian¹, L. C. Maximon¹, and W. C. Parke¹

¹*Department of Physics, The George Washington University, Washington, D.C. 20052, USA.*

²*University of Adiyaman, Department of Physics, 02040, Adiyaman, Turkey.*

³*NASA Goddard Space Flight Center, Greenbelt, MD 20771, USA.*

20 September 2012

ABSTRACT

Using a wavelet decomposition technique, we have extracted the Hurst exponent for a sample of 46 long and 22 short Gamma-ray bursts (GRBs) detected by the Gamma-ray Burst Monitor (GBM) aboard the Fermi satellite. This exponent is a scaling parameter that provides a measure of long-range behavior in a time series. The mean Hurst exponent for the short GRBs is significantly smaller than that for the long GRBs. The separation may serve as an unbiased criterion for distinguishing short and long GRBs.

Key words: Gamma-ray bursts

1 INTRODUCTION

Our present understanding of complex astrophysical objects such as cataclysmic variables (CVs), active galactic nuclei (AGNs), and gamma-ray bursts (GRBs) comes nearly entirely from the temporal and spectral analyses of their photoemissions (with

* E-mail: maclach@gwu.edu (GAM)

some additional information coming from possible associations, such as host galaxies). In this paper we consider the temporal aspects of GRB light curves observed by the Gamma-Ray Burst Monitor (GBM) aboard the Fermi satellite. Many studies of the temporal properties of GRB light curves have been published, such as Nemiroff (2000); Norris et al. (2005); Hakkila & Nemiroff (2009); Hakkila & Preece (2011); Nemiroff (2012), from the perspective that light curves are comprised of a series of displaced pulses and that by fitting the individual pulses and associating pulses at various photon energies one can arrive at a holistic understanding of light curves which in turn may be used to constrain the physics of the engines that produce them. The main appeal of this approach is the intuitive connection between pulses and collisions in the internal shock model. While this is a perfectly reasonable method, issues do arise concerning the functional form to use for pulse fitting and how to discern actual pulses from stochastic fluctuations in the light curves. The situation is further exacerbated by the fact that GRB light curves exhibit considerable variation in duration and in pulse profile. We note the significant progress made in non-parametric analyses using the Bayesian block technique (Scargle et al. 2012). In this type of analysis the duration of a light curve is represented as a tessellated block of time which can be partitioned into a complete array of sub-blocks in any number of ways. An optimal partition (a partition of sub-blocks maximizing a fitness function) is shown to exist, be unique, and computable iteratively. The optimal partition of sub-blocks is determined, given a prior probability distribution for the number of blocks, by finding the model best representing the data as sets of piece-wise constant segments or sub-blocks. This technique shows great promise in resolving statistically significant temporal features from noise and detector related artifacts.

An ideal complementary approach to probing light curves would be one which handles seemingly disparate profiles on an equal footing and distills their complex forms into a single parameter which may be used to compare one light curve with another. One such method was pioneered by Harold Edwin Hurst in 1951 with a technique he invented called the rescaled range analysis (R/S) which was later improved upon by Benoit Mandelbrot. The eponymous parameter resulting from the rescaled range analysis is called the Hurst exponent, H , and is closely related to the fractal dimension, D , the understanding of which Mandelbrot spent much of his career developing. In fact, fractional Brownian motion (fBm), which Mandelbrot defined in 1968, is parametrized solely by H and serves as a useful model for discussing time series. After determining H for a given time series one is in a position to make several statements about the nature of that time series including whether the sequence appears random or whether it is persistent or anti-persistent, and if it is, whether it exhibits long-range dependence, and over what time scales these characteristics are operative. All of these are informative quantitative statements, especially if the specific process generating the time series is partially or completely unknown, in which case, these statements are perhaps all one can really say about the process given the available information. Some fields of research in which interesting work is being done with Hurst exponents are financial markets, seismology, anesthesiology, astrophysics, plasma physics and genomics.

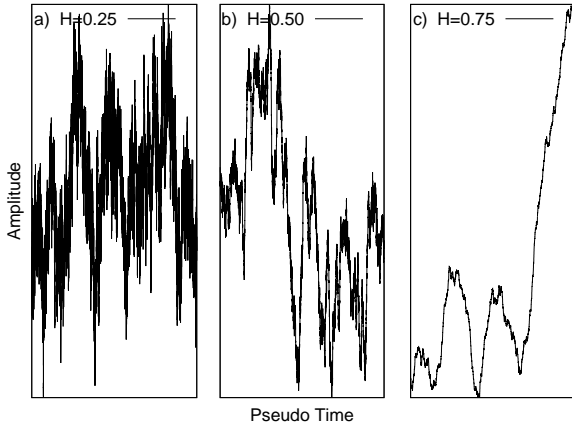


Figure 1. Simulated fractional Brownian motions with different values of H : a) $H = 0.25$, b) $H = 0.50$, c) $H = 0.75$.

We point out that neither the pulse fitting methods nor the Bayesian block analysis (Scargle et al. 2012) yields information directly relatable to the Hurst exponent as does the wavelet analysis. One approach to access the Hurst exponent from a Bayesian block framework that seems reasonable would be an adaptation of the Box-Counting algorithm (Feder 1988). Such a Bayesian-Box-Counting algorithm is outside the scope of this paper.

The estimation of the Hurst exponent and the related scaling exponent, α , has a history in astrophysics (Anzolin et al. 2010; Tamburini et al. 2009; Walker & Schaefer 2000; Fritz & Bruch 1998) for both Cataclysmic Variables (CVs) and GRBs. We propose that a similar determination of H for GRB light curves will be a valuable tool for categorization and we present a separation of long and short GRBs based on H .

2 METHODOLOGY

2.1 Hurst Exponent and Self-Affinity

Pioneering work in self-similarity and long-range dependence was first published in 1951 by Hurst in the study of annual Nile River levels, (Hurst 1951). Hurst examined several decades of data to determine what should be the minimum size of a reservoir so that it neither overflows nor runs dry due to yearly fluctuations and made the unexpected observation that annual Nile River levels were not independent from one another but instead exhibited a *memory* of past events.

In this analysis of time-series data we search for statistical fractals, i.e., fractals whose statistical characteristics are independent of time scale. Such fractal time-series are called *self-similar*. There is another class of statistical fractals whose scale invariance is broken but can be restored by a multiplicative factor. These statistical fractals are called *self-affine*. Mandelbrot (1985) defined a time-series, $X(t)$ with $t \in \{t_0 \dots t_{N-1}\}$, to be self-affine if, after a rescaling $t \rightarrow \lambda t$ the following

relation is satisfied,

$$X(t) \doteq \lambda^{-H} X(\lambda t). \quad (1)$$

The exponent, H , is the Hurst exponent, (Hurst 1951) and the symbol \doteq denotes equality in distribution. The canonical example of a self-affine time-series, also given by Mandelbrot (1968), is fractional Brownian motion, fBm. Stationary in the context of this paper is second-order stationarity which means the first and second moments obey the following relations

$$\begin{aligned} \mathbb{E}\{X(t)\} &= \mu_X \\ \mathbb{E}\{X(t_2)X(t_1)\} &= \gamma(t_2 - t_1) = \gamma(\tau), \end{aligned} \quad (2)$$

where μ_X is the sample-mean, γ is the auto-covariance sequence and $\tau \equiv t_2 - t_1$ is the lag. The Hurst exponent, H , parametrizes the degree of statistical self-similarity which a time-series exhibits. A self-similar series may be sub-divided into three categories: A series with $1/2 < H < 1$ is referred to as persistent or long-range dependent while a series with $0 < H < 1/2$ is referred to as anti-persistent, Feder (1988). For $H = 1/2$ we have neither persistence nor anti-persistence and this corresponds to the case of random and uncorrelated events. The Hurst exponent provides a model-independent characterization of the data. Three examples of times series with different values of H are shown in Fig. 1. A graphical depiction of the rescaling described by Eq. 1 for a time series with $H = 0.25$ is given in Fig. 2 and for a time series with $H = 0.75$ in Fig. 3.

2.2 Wavelet Transforms

Wavelet transformations have been shown to be a natural tool for multi-resolution analysis of non-stationary time-series (Flandrin 1992; Mallat 1989). Wavelet analysis is similar to Fourier analysis in many respects but differs in that a wavelet basis function, $\psi(t)$, is well-localized while Fourier basis functions are global. Localization means that outside some range the amplitudes of wavelet basis functions go to zero or are otherwise negligibly small, Percival (2000). On the other hand, the wavelet transform is similar to the Fourier transform because they both are expansions into a complete orthogonal basis and resolve low-frequency, large scale structure from high-frequency, small scale structure.

Wavelet analysis is said to be multiresolution because the time-series under investigation is interrogated at multiple scales by a basis set of wavelets which are rescaled and translated versions of an original wavelet commonly referred to as the mother-wavelet, $\psi(t)$,

$$\psi(t) \rightarrow \psi_{a,b}(t) = \frac{1}{\sqrt{a}} \psi\left(\frac{t-b}{a}\right), \quad (3)$$

where a represents an octave or time-scale and the parameter b gives the position of the wavelet within the octave.

The continuous wavelet transform (CWT) coefficient, $C_{a,b}$, of a time-series for some scale and position is computed as

$$C_{a,b} = \frac{1}{\sqrt{a}} \int X(t) \psi_{a,b}(t) dt. \quad (4)$$

2.2.0.1 Wavelet Analysis The wavelet-transform technique for estimating self-affinity is outlined here. By substituting the distribution relation in Eq. 1 into Eq. 4 we find

$$\begin{aligned} C_{a,b} &= \frac{1}{\sqrt{a}} \int X(t) \psi_{a,b}(t) dt \\ &= \frac{\lambda^{-(H+1/2)}}{\sqrt{\lambda a}} \int X(\lambda t) \psi_{a,b}\left(\frac{\lambda t - \lambda b}{\lambda a}\right) d(\lambda t) \\ &= \lambda^{-(H+1/2)} C_{\lambda a, \lambda b}. \end{aligned} \quad (5)$$

It is straightforward to see from Eq. 5 that a self-affine time-series will have wavelet coefficients whose variance over a particular scale, λa , is related to the scale parameter λ by,

$$\log \text{var}(C_{\lambda a, \lambda b}) = (2H + 1) \log \lambda + \text{constant}. \quad (6)$$

2.2.0.2 Fast Wavelet Transforms Similar to the CWT, the discrete fast wavelet transform (FWT) is also a multiresolution operation owing to the construction of the wavelets, $\psi_{j,k}$, which form the basis of the discrete fast wavelet transform. We employed the discrete wavelet transform because of its high degree of computational efficiency. In order to distinguish between the CWT and its FWT counterpart we make a slight change of notation. Just as before, the $\psi_{j,k}$, are rescaled, translated versions of the mother wavelet, ψ ,

$$\psi_{j,k} = 2^{-j/2} \psi(2^{-j}t - k). \quad (7)$$

The coefficients of the FWT are written as

$$d_{j,k} = \langle X, \psi_{j,k} \rangle,$$

where j and k play the roles of a and b , respectively. Moreover, the values which j and k assume obey the dyadic partitioning scheme (Mallat 1989; Addison 2002; Percival 2000). That is, for a time series whose number of elements is given by $N = 2^m$,

$$0 \leq j \leq m - 1,$$

and

$$0 \leq k \leq 2^j - 1.$$

Applying the dyadic partitioning scheme removes any redundant encoding of information by the wavelet transform coefficients and guarantees orthogonality among the wavelet basis for any change in j or k ,

$$\langle \psi_{j,k}, \psi_{j',k'} \rangle = \delta_{j,j'} \delta_{k,k'}. \quad (8)$$

2.3 Logscale Diagrams

The average power of the light curve at time scale j is expressed as β_j and may be written in terms of the variance of the FWT coefficients as

$$\beta_j = \text{var}(d_{j,k}) = \frac{1}{n_j} \sum_{k=0}^{n_j-1} |d_{j,k}|^2, \quad (9)$$

where n_j is the number of coefficients at scale, j , (Abry et al. 2000, 2003). Similarly to Eq. 6, it has been shown by Flandrin (1992) that for a series with non-stationary statistics the power-law variance of wavelet coefficients goes like

$$\log_2(\beta_j) = (2H + 1)j + \text{constant}, \quad (10)$$

where H is the Hurst exponent. Masry (1993) later extended this result to a larger class of non-stationary problems with stationary increments in the low-frequency limit and showed that fBms are a special case. A plot of Eq. 10 is referred to as a logscale diagram. Logscale diagrams are useful for identifying scaling regions, i.e., the range of octaves over which self-affine scaling occurs. The slope, α , of the scaling region determines related to the Hurst exponent through $\alpha = 2H + 1$.

2.4 Choice of Wavelet Basis

As in any orthogonal transformation, the basis functions to use in a wavelet transform is a matter of strategic choice. One typically chooses a basis that emphasizes some characteristic of interest. Commonly used families of wavelet bases are the Coiflet, Daubechies, and Haar (Addison 2002). We chose the Haar wavelet basis which is the simplest of the Daubechies family.

The Haar wavelet basis was chosen from among all other possible bases because it has the fewest number of vanishing moments and most compact support (Addison 2002), has a straightforward interpretation, i.e., is equivalent to the Allan variance (Xizheng & Zhensen 1997) and is constant over its interval of support similar to the model assumed in the Bayesian block method (Scargle 1998; Scargle et al. 2012).

The Haar basis is not without some defects, as noted by Kaplan & Jay Kuo (1993) and Flandrin (1992). Namely, the Haar wavelet transformation is known to underestimate the actual Hurst exponent and this phenomenon is a function of the coarseness of the binning, the number of counts in the light curve, and also of H itself. We show in Sec. 2.6 that this effect

is present but smaller than $\approx 1\sigma$ for a set of simulated light curves and is likely to be smaller for actual data. However, we consider that the advantages of the Haar basis outweigh its disadvantages.

2.5 Minimizing Uncertainties

2.5.1 Circular Permutation

Spurious artifacts due to incidental symmetries resulting from accidental misalignment (Percival 2000; Coifman 1995) of light curves with wavelet basis functions are minimized by circularly shifting the light curve against the basis functions. Circular shifting is a form of translation invariant de-noising (Coifman 1995). It is possible a shift will introduce additional artifacts by moving a different symmetry into a susceptible location. The best approach is to circulate the signal through all possible values, or at least a representative sampling, and then take an average over the cases which minimizes the effect of spurious correlations.

2.5.2 Reverse-Tail Concatenation

Both discrete Fourier and discrete wavelet transformations imply that the expansion is periodic, with the longest period equal to the full time range of the input data. This can be interpreted to mean that for a series of N elements, $\{X_0, X_1 \dots X_{N-1}\}$ then X_0 is made a surrogate for X_N and X_1 is made a surrogate for X_{N+1} , and so forth. This assumption may lead to trouble if X_0 is much different from X_{N-1} . In this case, artificially large variances may be computed. Reverse-tail concatenation minimizes this problem by making a copy of the series which is then reversed and concatenated onto the end of the original series resulting in a new series with a length twice that of the original. Instead of matching boundary conditions like,

$$X_0, X_1, \dots, X_{N-1}, X_0, \tag{11}$$

we match boundaries as,

$$X_0, X_1, \dots, X_{N-1}, X_{N-1}, \dots, X_1, X_0. \tag{12}$$

Note that the series length has thus artificially been increased to $2N$ by reversing and doubling of the original series. Consequently, the wavelet variances at the largest scale in a logscale diagram reflect this redundancy. This is the reason that the wavelet variances at the largest scale are excluded from least-squares fits of the scaling region.

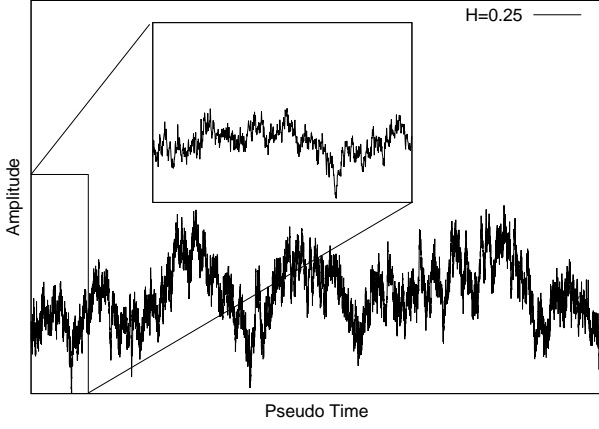


Figure 2. Graph of $B_H(t)$ with $H = 0.25$. A box is placed around a sub-range of t (lower left hand corner). The box is zoomed into with time axis scaled by a and amplitude scaled by a^{-H} . This is a *self-affine* transformation that not only makes the rescaled version qualitatively 'similar' to the original but also preserves the variance as computed in Eq. 9.

2.5.3 Poisson Operator

Photon counting statistics are considered in a bootstrapping procedure by applying a Poisson operator, $\mathcal{P}(\lambda_i, X_i)$, to every light curve prior to analyzing. Each light curve is binned initially at 200 μ -seconds and the number of counts per bin, X_i , is used as a mean value, λ_i , to be supplied to a Poisson random number generator. The value returned from $\mathcal{P}(\lambda_i, X_i)$ is used to replace the number of counts stored in X_i . The Poisson operator is applied to the signal X_i prior to every circular permutation. We show in Sec. 2.6 that the Poisson operator does not affect the measured slope of logscale diagrams above the Poisson level.

2.6 A Test Case: Fractional Brownian Motion

Spatial-temporal fractional Brownian motions (fBm's) are a useful model for studying self-similarity and long-range dependence in non-stationary time-series, Mandelbrot (1968) and are characterized by a single parameter, H , the Hurst exponent. An fBm with a particular H is expressed as $B_H(t)$ and has the property of self-similarity over a range of scales after a rescaling of axes,

$$B_H(t) \doteq a^{-H} B_H(at), \quad (13)$$

where \doteq denotes distributional equality as in Section 2.1. The efficacy of the H estimation procedure was tested using simulated data in the form of fractional Brownian motion (fBm) time series. Two tests were performed; in the first test we examine the ability of our algorithm to determine H from fBms in the presence of Poisson noise and in the second test we examine how well we can determine H at $H = 0.25$, $H = 0.50$, and $H = 0.75$ from noise-free fBms.

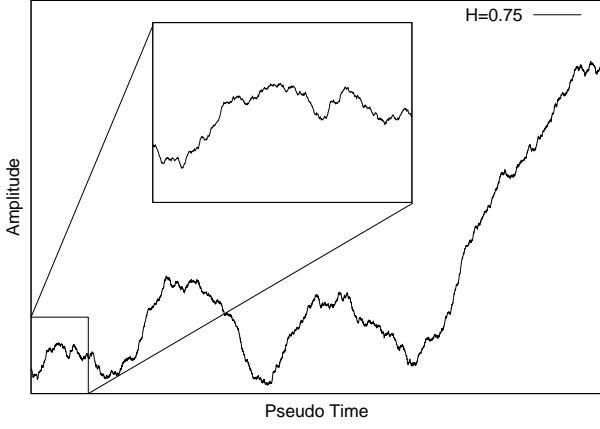


Figure 3. Graph of $B_H(t)$ with $H = 0.75$. A box is placed around a sub-range of t (lower left hand corner). The box is zoomed into with time axis scaled by a and amplitude scaled by a^{-H} . This is a *self-affine* transformation that not only makes the rescaled version qualitatively 'similar' to the original but also preserves the variance as computed in Eq. 9.

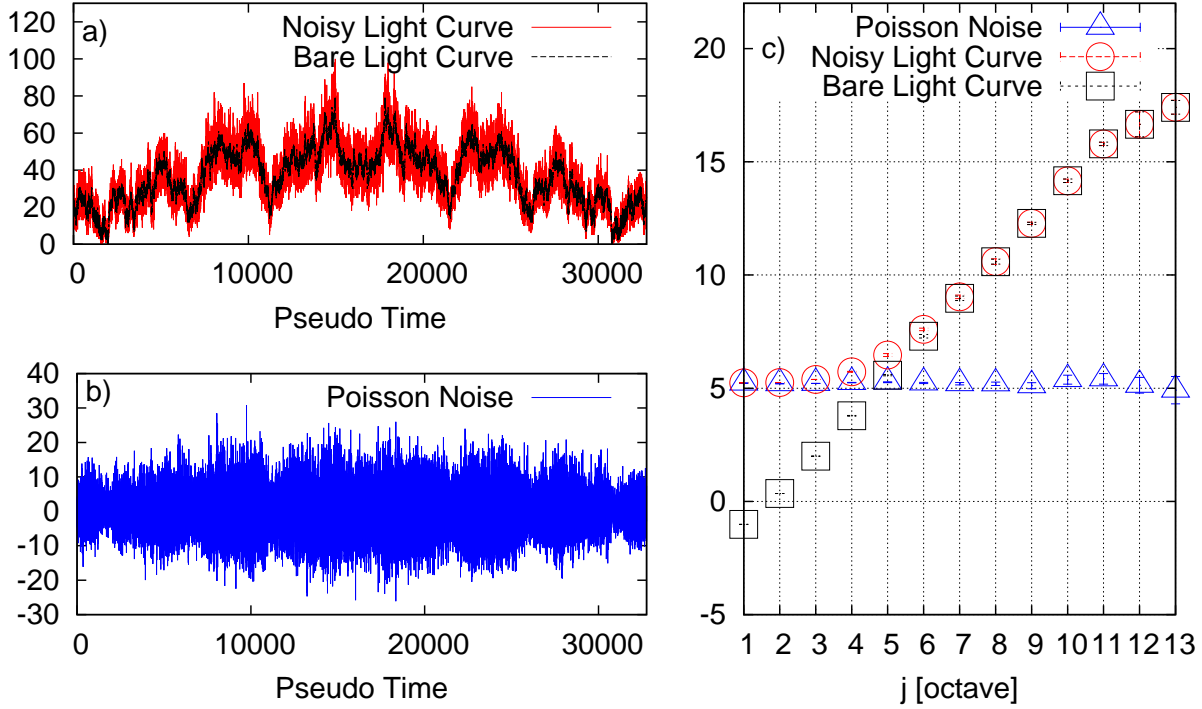


Figure 4. Panel a) shows a sample fBm pre-processed and ready to be analyzed in black and the same light curve after applying the Poisson operator, \mathcal{P} , in red. Panel b) shows the Poisson noise that has been added by \mathcal{P} . In panel c) logscale diagrams illustrate the effect of Poisson statistics on the Hurst exponent. The bare fBm is shown in black, the dressed Poisson-type fBm is in red, and the residual Poisson noise is shown in blue.

2.6.1 Test 1

The numerical computing environment MATLAB was used to produce 1000 realizations of fBms with scaling parameter H randomly chosen from the range $0.0 < \alpha < 1.0$ by using a uniform random number generator. Copies of the fBms were combined with a Poisson operator as described in Sec. 2.5.3. The fBms and the Poissonian fBms thus produced are shown in black and red respectively in panel a) of Fig. 4. Panel b) shows the Poisson noise that has been added by \mathcal{P} . The Logscale

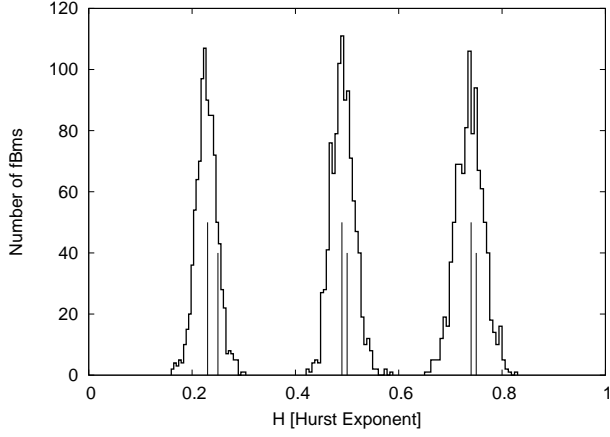


Figure 5. Histograms of 3000 simulated fBm traces. Three categories of fBms were generated with known Hurst exponents, $H = 0.25$, $H = 0.50$, and $H = 0.75$. These fBms were then analyzed to recover the Hurst exponent. The histograms are the results of this analysis. Pairs of vertical lines are drawn for each peak. The shorter of the two indicates the known H used to generate the fBms and the longer of the two indicates the H extracted by our analysis. Results are tabulated in Table 1.

diagrams in panel c) illustrate the effect of Poisson statistics on the Hurst exponent. The bare fBm is shown in black, the dressed Poisson-type fBm is in red, and the residual Poisson noise is shown in blue. The logscale diagram for the bare fBm in panel c) exhibits a clean slope across all octaves. We see the effect of a Poisson noise operator; it adds to the signal variance, constant across all octaves. Below some octave the signal is completely dominated by noise but above that octave the slope of the logscale diagrams is independent of \mathcal{P} . See for example the black and red symbols for $j \geq 6$.

2.6.2 Test 2

In the second test, 3000 simulated Poisson-type light curves were generated. The simulated data were divided into three subgroups of 1000 according to H . The three subgroups were $H = \{0.25, 0.50, 0.75\}$. The simulated data in each group were analysed and an attempt was made to recover the value of the Hurst exponent, H , used to generate the fBm. The Hurst exponent was estimated by a least squares fit to the scaling portion of the logscale diagrams to determine α and then H is found from Eq. 10.

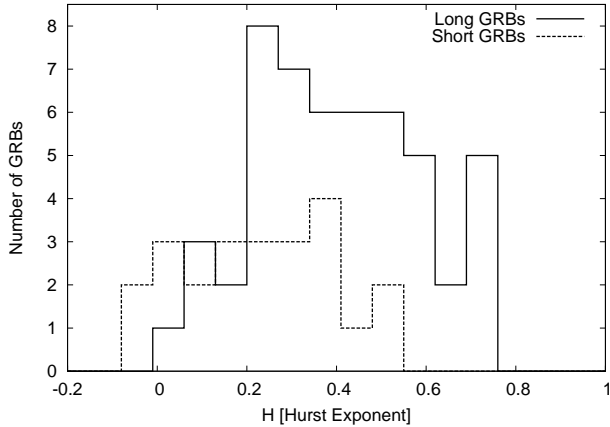
Results of the second test can be seen in Fig. 5 and Table 1. The results show that the FWT analysis with the Haar wavelet basis does underestimate the value of H as discussed in Sec. 2.4 but the magnitude of the error is not significant for our purpose.

3 DATA REDUCTION

The Gamma-Ray Burst Monitor (GBM) on board Fermi observes GRBs in the energy range 8 keV to 40 MeV. The GBM is composed of 12 thallium-activated sodium iodide (NaI) scintillation detectors (12.7 cm in diameter by 1.27 cm thick) that

Table 1. Summary of results in Fig. 5.

H	H_{meas}
0.25	0.23 ± 0.02
0.50	0.49 ± 0.02
0.75	0.74 ± 0.03

**Figure 6.** Histogram of H extracted from long and short GRBs. The result for long GRBs is plotted as the solid line while the short GRB result is plotted with the dashed line. Note the overlap but also that the means are displaced from one another.

are sensitive to energies in the range of 8 keV to 1 MeV, and two bismuth germanate (BGO) scintillation detectors (12.7 cm diameter by 12.7 cm thick) with energy coverage between 200 keV and 40 MeV. The GBM detectors are arranged in such a way that they provide a significant view of the sky (Meegan et al. 2009).

In this work, we have extracted light curves for the GBM NaI detectors over the entire energy range (8 keV - 1 MeV, also including the overflow beyond 1 MeV). Typically, the brightest three NaI detectors were chosen for the extraction. Lightcurves for both long and short GRBs were extracted at a time binning of 200 microseconds. The long GRBs were extracted over a duration starting from 20 seconds before the trigger and up to about 50 seconds after the T_{90} for the burst without any background subtraction. For short GRBs, durations were chosen to be 20 seconds before the trigger and 10 seconds after the T_{90} . The T_{90} durations were obtained from the Fermi GBM-Burst Catalog (Paciesas et al. 2012). Summaries for the 46 long and 22 short GRBs used in this study are tabulated in Tables 2 and 3.

4 RESULTS AND DISCUSSION

We have used a technique based on wavelets to determine the Hurst exponents for a sample of GRB prompt-emission light curves. As noted in Section 2.1, the Hurst exponent provides a measure of correlated (or long-range) behavior in a time series. The extreme values of H vary from 0 to 1, and a value of 0.5 implies uncorrelated (random) behavior. As the fBm

model indicates, large H values tend to be associated with relatively smooth functions and small H values tend to favor highly jagged curves. This feature suggests that H may be useful in quantifying the variability observed in GRB prompt-emission light curves. Plotted in Fig. 6 are the extracted H -exponents as histograms for both long and short GRBs. The histograms clearly show a displacement in H for the distributions of long and short GRBs, with the short GRBs indicating a preference for small values of H . The mean displacement in H raises the interesting possibility of using this feature as a way of distinguishing between short and long GRBs. This would be in addition to the currently employed criteria based on T90 and spectral hardness ratios. Interestingly, the histograms also show a significant overlap in the region of small H exponents possibly signaling similarities between the two types of bursts in this range.

It could be argued that the sizable overlap of the distributions is essentially a consequence of the large dispersion (in H) exhibited by both short and long GRB distributions. While it is not known precisely what processes lead to this large dispersion in H , we note that the dispersion for the short GRBs is somewhat smaller than the corresponding one for long GRBs. If the dispersion is associated with the energetics of the progenitors of the respective systems, i.e., a merger of compact objects in the case of short GRBs and the collapse of a rapidly rotating massive star for long GRBs, then one might indeed expect a larger dispersion in the H -distribution of long GRBs compared to the corresponding one for short GRBs based purely on the difference in the mass range for the respective progenitors. Moreover, additional factors such as the formation of an accretion disk, the size of the disk, the mass of the disk, the strength of the magnetic field and the magnitude of the accretion rate during the prompt phase, remain largely uncertain. With the added intrinsic variability of the central engine itself, we should not be surprised to observe a systematic difference in the extracted Hurst exponents for long and short bursts. For completeness, we mention that while the dispersion in H is large for both distributions, the extracted H -value for each individual GRB is known reasonably precisely (see Table 1).

Another way to examine the H -distributions is to recast the data against the so-called minimum-time-scale parameter, MTS, extracted by MacLachlan et al. (2012) and MacLachlan et al. (2012a). Using a method based on wavelets, these authors explored the scaling characteristics of GRBs and determined the minimum time scale at which scaling processes dominate over random noise processes. Furthermore, the authors have recently shown a direct connection between the extracted MTS and the smallest pulse structures extracted by pulse-fitting techniques. In addition to this link with pulses, MTS provides an alternate scale (to T_{90}) by which long and short GRBs can be separated. Shown in Fig. 7 are the extracted H -exponents for both long and short GRBs versus the MTS (in the observer frame). Short GRBs tend to cluster around small MTS values and follow a steep trajectory in the H -MTS plane whereas the long GRBs are distributed over a larger range in MTS and seem to follow a gradual power-law-like trajectory. The behavior is a little more clear in panel (b) of Fig. 7 where the MTS is plotted

on a log scale: Here the the short and long GRBs indicate a small ($\sim 30\%$) positive correlation respectively; the combined sample on the other hand shows a larger positive correlation ($\sim 50\%$) and an obvious separation of the two distributions with MTS.

Other astrophysical systems for which the Hurst exponent has been extracted includes CVs. These systems, comprising tightly-bound binaries (with periods of the order of few hours) and a primary consisting of a compact object (typically a white dwarf) and an accretion disk that can accommodate significant mass transfer from the secondary may provide a benchmark for gauging the systematics of the extracted Hurst exponents. Indeed, large dispersions in H are found for both optical and X-ray light curves of CVs. Interestingly though, CVs apparently tend to favor large H -exponents i.e., greater than 0.5. This implies that the CV distributions are persistent as opposed to a tendency toward antipersistence for GRBs. By their very nature, CVs are systems that have built-in periodicity that is readily reflected, in most cases, in the observed emissions from these systems. GRBs, on the other hand, are transient phenomena which show very little evidence for periodicities. It's possible this simple difference may lead, in part at least, to the degree of persistence or antipersistence exhibited by these systems. Furthermore, some authors, (Fritz & Bruch 1998; Tamburini et al. 2009; Anzolin et al. 2010), have noted that the extracted H 's indicate a sensitivity to the strength of the magnetic field of the systems under study, and in particular, the optical and x-ray emissions from CVs exhibit different H distributions. Since the optical and x-ray emissions in CVs arise from spatially separated regions (the optical from an extended disk and the x-ray in the boundary layer between the inner regions of the disk and the surface of the compact object or the polar regions in the case of a highly magnetic system), it is tempting to surmise that such a comparison might be fruitful in elucidating the spatial characteristics of GRB jets: Examples include the radii and or regions that are commonly associated with the emission sites for prompt gamma-rays (e.g., the photospheric radius in the case of a thermal component) and the steeply declining phase of the x-ray light curves (linked with high-latitude emission resulting from internal shell collisions). While it is understood that GRBs and CVs are very different systems and therefore the translation of the Hurst exponent from one system to the other is likely to be speculative at best, it is intriguing nonetheless that a simple scaling parameter may enable us to connect common underlying properties and processes that ultimately produce the observed emission in these diverse systems.

5 CONCLUSIONS

We have studied the temporal properties of a sample of prompt-emission light curves for short and long-duration GRBs detected by the Fermi/GBM mission. By using a technique based on wavelets we have extracted the Hurst exponents for

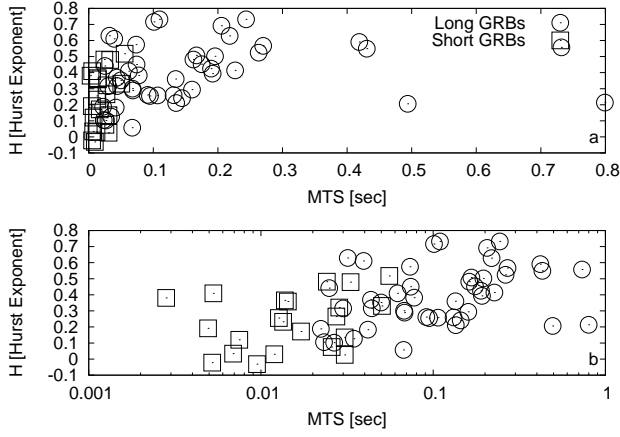


Figure 7. A scatter plot of H against the minimum variability time scale from MacLachlan et al. (2012) and MacLachlan et al. (2012a).

these bursts. This exponent is essentially a scaling parameter that provides a measure of long-range behavior in a time series. The physical limits of this index are 0 and 1, where the mid-point ($H = 0.5$), is an indicator of completely uncorrelated (random) processes that contribute to the observed time series. Often times, the H is also associated with the fractal dimension (D) of structures by

$$D = 2 - H, \quad (14)$$

and can be thought of as a measure of the degree of jaggedness of the structures under study. In this sense the H may also be indirectly linked to the variability seen in the prompt-emission of many GRBs. Our main results are summarized as follows:

a) The means of the H distributions for the GRBs in our sample show an offset between short and long GRBs, with the short GRBs indicating a preference for smaller Hurst exponents compared to the long GRBs. This offset is potentially an independent criterion for distinguishing between long and short-duration bursts.

b) Compared to short GRBs, long-duration bursts exhibit a larger dispersion in H . The origin of this dispersion is not known although it is possible that it is related to the underlying energetics of the different progenitors that produce long and short-duration bursts.

c) No distinct group or clustering is found for H values corresponding to 0.5. This implies that random (or uncorrelated) processes, if present, play a lesser role in the production of the observed prompt emission. Moreover, the means of the H -distributions for both long and short GRBs indicate a skewness toward values less than 0.5. Overall, this implies that the prompt-emission time series exhibit antipersistence.

Finally, we note that because of the large dispersion in H , there exists a significant region over which the long and short bursts overlap. This overlap region raises the interesting possibility of exploring bursts that may possess many more common

features than would otherwise be suspected. The case for an intermediate class of GRBs (Horvath 1998; Gao et al. 2010) remains unsettled and warrants further investigation.

6 ACKNOWLEDGEMENTS

The NASA grant NNX11AE36G provided partial support for this work and is gratefully acknowledged. The authors (GAM and KSD) acknowledge very useful discussions with Tilan Ukwatta.

REFERENCES

- Abry P., Flandrin P., Taqqu M. S., & Veitch D., 2000, *Self-Similar Network Traffic and Performance Evaluation*, pg 39–88, New York: Wiley, K. Park and W. Willinger
- Abry P., Flandrin P., Taqqu M. S., & Veitch D., 2003, *Theory and Applications of Long-Range Dependence*, Boston: Birkhauser, 527–556
- Anzolin G., Tamburini F., De Martino D., Bianchini A., 2002, *A&A*, 519, A69
- Addison P. S., 2002, *The Illustrated Wavelet Transform Handbook*, IOP Publishing Ltd.
- Coifman R. R., Donoho D. L. 1995, Springer-Verlag, 125–150
- Feder J., 1988, *Fractals*, Plenum Press
- Flandrin P., 1989, IEEE, Transactions on Information Theory, 35, 197–199
- Flandrin P., 1992, IEEE, Transactions on Information Theory, 38, 910–917
- Fritz T., Bruch A., 1998, *A&A*, 332, 586–604
- Gao H., Lu Y., & Zhang S. N., 2010, *ApJ*, 717, 268
- Hakkila J. & Nemiroff R. J. 2009, *ApJ*, 705, 372
- Hakkila J. & Preese R. 2011, *ApJ*, 740, 104
- Horvath I., 1998, *ApJ*, 508, 757
- Hurst H. E., 1951, Trans. Am. Soc. Civ. Eng., 116, 770
- Kaplan L. C., Jay Kuo C. C., 1989, IEEE, Transactions on Signal Processing, 41, 3554–3562
- MacLachlan G. A., et al. 2012, arXiv:1201.4431 [astro-ph.HE] (Submitted to *MNRAS*)
- MacLachlan G. A., Shenoy A., Sonbas E., Dhuga K. S., Eskandarian A., Maximon L. C., Parke W. C., 2012, *MNRAS Letters* (online version)

- Mallat S. G., 1989, IEEE, Transactions on Pattern Analysis and Machine Intelligence, 11, 674–693
- Mandelbrot B. B. and Van Ness J. W. 1968, SIAM Review, 10, 422–437
- Mandelbrot B. B, SIAM Review, vol. 10, 1968, pg 422–437
- Masry E., IEEE, Transactions on Information Theory, vol. 39, 1993, pg. 260–264
- Meegan C. et al. 2009, *ApJ*, 702, 791
- Nemiroff R. J. et al. 2000, *ApJ*, 544, 805
- Nemiroff R. J. 2012, *MNRAS*, 419, 1650
- Norris J. P. et al. 2005, *ApJ*, 627, 324
- Paciesas W. S. et al. 2012, arXiv:1201.3099v1 [astro-ph.HE].
- Percival D. B. and Walden A. T. 2002, *Wavelet Methods for Time Series Analysis*, Cambridge University Press
- Scargle J. D., 1998, *ApJ*, 504, 405–418
- Scargle J. D., Norris J. P., Jackson B., Chiang J., 2012, arXiv:1207.5578v2 [astro-ph.IM]
- Tamburini F., De Martino D., & Bianchini A., 2009, *A&A*, 502, 1,1–5
- Walker K. C., Schaefer B., 2000, *ApJ*, 537, 264
- Xizheng K., Zhensen W., 1993, Frequency Control Symposium, 1997., Proceedings of the 1997 IEEE International, 515–518

Table 2. Summary of Long GRBs.

GRB Number	H	δH	T_{90} [sec]	δT_{90} [sec]
080723557	0.316	0.023	58.369	1.985
080723985	0.425	0.053	42.817	0.659
080724401	0.451	0.060	379.397	2.202
080804972	0.549	0.085	24.704	1.460
080806896	0.591	0.056	75.777	4.185
080807993	0.105	0.014	19.072	0.181
080810549	0.211	0.037	107.457	15.413
080816503	0.258	0.035	64.769	1.810
080817161	0.393	0.048	60.289	0.466
080825593	0.382	0.036	20.992	0.231
080906212	0.716	0.070	2.875	0.767
080916009	0.414	0.053	62.977	0.810
080925775	0.453	0.056	31.744	3.167
081009140	0.732	0.073	41.345	0.264
081101532	0.255	0.040	8.256	0.889
081125496	0.629	0.080	9.280	0.607
081129161	0.261	0.036	62.657	7.318
081215784	0.629	0.070	5.568	0.143
081221681	0.567	0.089	29.697	0.410
081222204	0.502	0.065	18.880	2.318
081224887	0.692	0.071	16.448	1.159
090102122	0.126	0.013	26.624	0.810
090131090	0.575	0.062	35.073	1.056
090202347	0.241	0.039	12.608	0.345
090323002	0.294	0.025	135.170	1.448
090328401	0.289	0.034	61.697	1.810
090411991	0.057	0.017	14.336	1.086
090424592	0.442	0.029	14.144	0.264
090425377	0.360	0.047	75.393	2.450
090516137	0.206	0.026	118.018	4.028
090516353	0.214	0.104	123.074	2.896
090528516	0.259	0.026	79.041	1.088
090618353	0.524	0.053	112.386	1.086
090620400	0.508	0.052	13.568	0.724
090626189	0.352	0.025	48.897	2.828
090718762	0.482	0.055	23.744	0.802
090809978	0.732	0.124	11.008	0.320
090810659	0.558	0.104	123.458	1.747
090829672	0.300	0.029	67.585	2.896
090831317	0.102	0.013	39.424	0.572
090902462	0.188	0.014	19.328	0.286
090926181	0.369	0.032	13.760	0.286
091003191	0.316	0.033	20.224	0.362
091127976	0.611	0.060	8.701	0.571
091208410	0.409	0.031	12.480	5.018
100414097	0.183	0.020	26.497	2.073

Table 3. Summary of Short GRBs.

GRB Number	H	δH	T_{90} [sec]	δT_{90} [sec]
080723913	0.026	0.008	0.192	0.345
081012045	-0.022	-0.002	1.216	1.748
081102365	0.075	0.011	1.728	0.231
081105614	0.135	0.026	1.280	1.368
081107321	0.331	0.059	1.664	0.234
081216531	0.366	0.046	0.768	0.429
090108020	0.482	0.048	0.704	0.143
090206620	0.358	0.042	0.320	0.143
090227772	0.409	0.038	1.280	1.026
090228204	0.381	0.027	0.448	0.143
090308734	0.030	0.004	1.664	0.286
090429753	0.321	0.045	0.640	0.466
090510016	0.192	0.017	0.960	0.138
090621922	0.255	0.053	0.384	1.032
090907808	0.265	0.034	0.832	0.320
091012783	0.120	0.014	0.704	2.499
100117879	0.479	0.046	0.256	0.834
100204858	0.518	0.070	1.920	2.375
100328141	0.034	0.005	0.384	0.143
100612545	0.171	0.021	0.576	0.181
100625773	0.232	0.041	0.192	0.143
100706693	-0.031	-0.009	0.128	0.143